**Reports in Mechanical Engineering**
Vol. 7, No. 1, 2026, pp. 253-272
ISSN: 2683-5894, DOI: https://doi.org/10.31181/rme553 

# Nested Planetary-Cycloidal Transmissions Design for Compact and Lightweight Exoskeletons Actuators

**Riccardo Bezzini[1*], Giulia Bassani[1], Carlo Alberto Avizzano[1], Alessandro Filippeschi[1]**
Institute of Mechanical Intelligence, Department of Excellence in Robotics and AI, Sant'Anna School of Advanced Studies, 56127, Pisa, Italy (IT)

**Article Info**

***Article history:***

Received February 13, 2026
Revised March 18, 2026
Accepted March 30, 2026

***Keywords:***
Exoskeletons,
Actuators,
Planetary,
Cycloidal,
Gearbox,
3D-Print

**ABSTRACT**

Recent progress in assistive exoskeleton technologies has demonstrated significant improvements in reducing users' metabolic cost and mitigating biomechanical overload. A key factor in achieving these outcomes lies in the design of the transmission systems, which must ensure efficiency, safety, and user comfort. Consequently, it is fundamental to develop compact, lightweight, and backdrivable gearboxes with low mechanical output impedance for wearable robotics. This paper presents two configurations of a novel nested Planetary-Cycloidal (PLACY) transmission system, which address the axial bulkiness limitations found in previous cycloid-planetary (CP) series implementations. The proposed architectures integrate a compact planetary stage, whose output element (the outer ring) is employed as an input shaft for two different cycloidal reducers. One implements a double-disk cycloidal design (PLACYd), while the other is realized according to the cycloidal compact-cam variant (PLACYc). These solutions enable high gear reduction ratios while maintaining minimal weights, low encumbrances, and backdrivability. Two 3D-printed prototypes are developed by employing the cycloidal non-pinwheel design and subjected to a comprehensive experimental characterization to assess their employment for wearable robotics actuators. Performance metrics were compared with those of the earlier CP designs and with other state-of-the-art 3D-printed and metal-built gearboxes to validate the developed prototypes' applicability to real-world assistive scenarios. Experimental results confirm that the proposed PLACY transmissions result in promising solutions for assistive exoskeletons, offering a favorable balance between high reduction ratio, compact form factor, and mechanical transparency.



***Corresponding Author:***

Riccardo Bezzini
Institute of Mechanical Intelligence, Department of Excellence in Robotics and AI, Sant'Anna School of Advanced Studies, 56127, Pisa, Italy (IT)
Email: riccardo.bezzini@santannapisa.it

## 1. Introduction

Wearable exoskeletons are human-assistive robotic systems designed to augment, restore, or assist motor capabilities by providing mechanical support to the user's limbs. They enable fundamental motor functions such as level walking, sit-to-stand transitions, and postural stability for individuals with neuromuscular disorders or mobility impairments (Karthik et al., 2025; Xu et al., 2025; Zhu et al., 2025). Achieving seamless and intuitive physical human-robot interaction (pHRI) requires actuation mechanisms characterized by low mechanical output impedance, high intrinsic backdrivability, and minimal reflected inertia (Laschowski & McPhee, 2023), delivering precise mechanical assistance while preserving ergonomic comfort and intuitive physical Human-Robot Interaction (pHRI). These attributes are critical to ensure compliant motion that aligns with the user's natural biomechanics while preserving responsiveness and safety. Furthermore, actuation units must comply with stringent constraints on size, mass, and volume to maintain ergonomic compatibility and overall wearability (Qian et al., 2022).

A primary engineering challenge in meeting these requirements lies in the design of the transmission system. In

wearable robotic applications, these systems must simultaneously achieve high torque density, low weight, compact geometry, mechanical efficiency, cost-effectiveness, and backdrivability (Calanca et al., 2020). Balancing these often-conflicting criteria remains a key challenge in the development of exoskeleton actuators. Several transmission architectures have been explored to address this design trade-off. Despite multiple actuation strategies have been explored to meet these technical requirements (Tiboni et al., 2022), including hydraulic (Fan et al., 2024) and pneumatic (Mišković et al., 2024) actuators, the bulkiness, complexity, and power supply constraints pose strict limitations on the suitability of wearable applications. In contrast, electric motor-driven systems coupled with mechanical reducers have emerged as the most popular choice due to their controllability, efficiency, and ease of integration (Rodríguez-Jorge et al., 2025; Xia et al., 2024). Quasi-direct drive (QDD) systems, widely adopted in human-centered robotics for their superior torque transparency and inherent backdrivability, represent one prominent approach (Huang et al., 2022; Yu et al., 2020). However, their low reduction ratios inherently limit achievable output torque. Among the different existing compact transmission technologies employed for exoskeleton actuation, cycloidal (Barsomian et al., 2024) and planetary (Jenks et al., 2025) reducers are particularly prominent, both separately and arranged in combined architectures (Bezzini et al., 2025; Yang et al., 2021). Cycloidal drives are valued for their high torque density and multiple simultaneous tooth engagement. However, these reducers typically present large radial dimensions and complex kinematics, which can hinder integration into wearable devices. Planetary gear trains, on the other hand, allow for the design of compact and efficient mechanisms, but are limited regarding the resulting achievable reduction ratios within a single stage (1:3 - 1:9)(Matsuki et al., 2019).

In our previous work (Bezzini et al., 2024), we designed and tested two hybrid Cycloidal-Planetary Series (CP) gearboxes, aiming to combine the advantages of both architectures. While this solution demonstrated promising mechanical properties in terms of torque handling, friction, back-drivability, and structural rigidity, the serial configuration of the two stages resulted in considerable weight and axial encumbrance, which restricted its applicability to tightly packaged wearable robots. To address the spatial limitations of the previous design, we propose a novel Nested Planetary-Cycloidal architecture (PLACY) specifically tailored for exoskeleton joint actuation.

The core of this architecture lies in embedding a compact planetary reduction stage, whose output (i.e., the outer ring rotation) is employed as input for the successive transmission phase, inside the eccentric shaft of a cycloidal reducer. This coaxial nesting seriously reduces the axial length of the resulting gearbox while maintaining the benefits of a high reduction ratio and mechanical robustness. The resulting configuration offers a streamlined form factor, improved torque density, and enhanced back-drivability-key attributes for wearable assistive devices, where actuator space and mass are highly constrained.

Although previous studies have investigated nested cycloidal configurations - such as the Three-Stage Cycloidal Nested (TSCN) gearbox introduced in (Maccioni et al., 2023), those designs rely entirely on cycloidal kinematics. While effective in compact high-ratio implementations, they often require a large number of rollers to meet torque requirements, leading to increased mass and cost. Furthermore, the TSCN architecture may struggle to maintain adequate backdrivability, a critical factor for pHRI.

To provide a thorough assessment of the PLACY-series architecture, this work first defines two alternative geometric and mechanical structures of the reducer, presenting two combinations that differ in the design of the outer cycloidal stage. One architecture employs a traditional double-disk cycloidal drive (addressed as PLACYd in the following) while the other utilizes the compact-cam variant (Lin et al., 2022) as the second stage of the mechanism (PLACYc). To facilitate the design and employment of this arrangement, an executable design tool is provided for assisting the designer in the choice of the geometric parameters, ensuring the compatibility between the successive Planetary and Cycloidal stages.

Two prototypes are developed by 3D-printing and evaluated across key performance metrics relevant to wearable robotics (Hartnett et al., 2025). These include gear play, torsional stiffness, internal friction, and back-drivability. Through this validation, the CP-series reducer is demonstrated to be a viable and efficient solution for wearable exoskeletons, offering a significant improvement in volumetric efficiency and mechanical transparency over previous hybrid gearbox designs. The architecture represents a strategic step forward in designing compact, high-performance actuators that meet the demanding requirements of human-centered robotics, holding the potential to overcome the trade-offs typically associated with high-ratio, compactness, and back-drivability in transmissions.

The main contributions of this paper are the following:

• The definition of two novel flat nested planetary-cycloidal transmissions that integrate a compact planetary stage within different cycloidal architectures. This design, conceived for compact and efficient integration in wearable assistive devices, enables high transmission ratios while guaranteeing significant backdrivability, reductions in weight, cost, and spatial encumbrance.

• The design of two 3D-printed prototypes implementing a 1:45 reduction ratio. An executable tool (and its Python source code) for the geometric design of custom PLACY reduction gearboxes is available at (Chen et al., 2008).

• The experimental assessment of the presented prototypes, evaluated both with respect to other state-of-the-art 3D-printed and metal-built gearboxes and to validate their use in an actuation module for assistive wearable devices.

The remainder of the paper is structured as follows: Section II presents the basic transmission designs employed to compose the PLACY architectures, describes the executable design tool functions, and presents the mechanical design and fabrication of the PLACY reducer prototypes. Then the experimental setup is presented, together with the selected evaluation metrics and respective test methodologies. Section III presents and discusses the obtained results, validating the PLACY designs' use in wearable assistive devices. Finally, Section IV concludes with insights and future directions for human-centered robotic transmissions.

## 2. Materials and Methods

### 2.1 Background

Before presenting the novel PLACY combinations, brief descriptions of the epicyclic planetary design, the classic cycloidal drive, and the compact-cam variation are presented in order to highlight their strengths and weaknesses.

#### 2.1.1 Epicyclic Planetary Stage

Planetary transmissions consist of four fundamental components: the sun gear, the planet gears, the carrier connected to the planets, and the outer ring gear, the latter being internally toothed. This class of mechanisms supports multiple operational modes, defined by the choice of fixed and rotating members. In standard configurations, only two of the three gear sets are permitted to rotate simultaneously. In the present work, the planetary stage is arranged with a stationary planet carrier, a driven sun gear serving as the input, and a ring providing the output. The gear ratio of a planetary transmission is governed by the difference in the number of teeth between the ring gear and the sun gear. Considering the following expressions, which represent the kinematic constraints associated with the sun-planet and planet-ring meshing interactions, respectively, the overall gear ratio of a general planetary configuration can be derived:

$$z_s\,\omega_s + z_p\,\omega_p - (z_s + z_p)\omega_c = 0 \tag{1}$$

$$z_r\,\omega_r + z_p\,\omega_p - (z_r + z_p)\omega_c = 0 \tag{2}$$

Where $z$ denotes the tooth count, $\omega$ the angular velocity, and the subscripts $s$, $p$, $r$, and $c$ correspond to the sun, planet, ring, and carrier, respectively. For the planetary gear sets, the following relation between tooth numbers holds:

$$z_r = z_s + 2\,z_p \tag{3}$$

Furthermore, because the planet carrier is fixed in the proposed gearbox designs, we impose $\omega_c = 0$. Consequently, the transmission ratio for the single-stage planetary reducers considered here is given by:

$$i_{pl} = \omega_r / \omega_s = -z_s / z_r \tag{4}$$

Simple epicyclic planetary stages generally realize gear ratios in the range of approximately 1:3 to 1:9. This inherent limitation becomes significant when substantially higher ratios are required, thereby motivating the use of compound planetary arrangements or multiple cascaded stages. Additionally, achieving larger ratios necessitates larger disproportions between planet gears relative to the sun gear, which considerably influences the reducer's overall volume and mass.

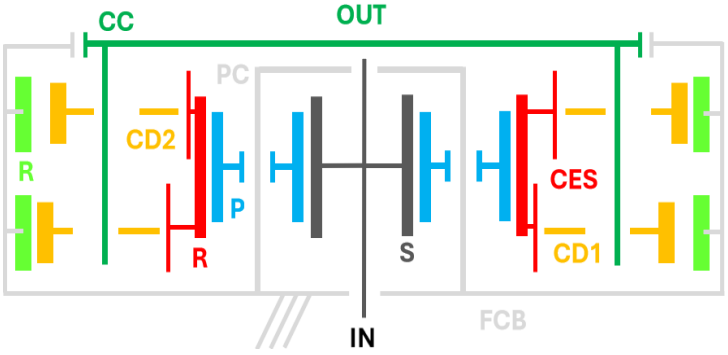


(a) PLACYd Architecture Schematic Illustration. The Planetary Stage is Embedded in the Input Shaft of a Double-disk Cycloidal Reducer

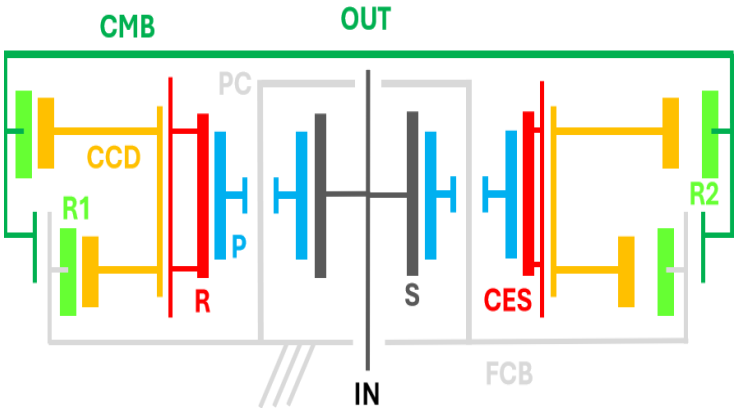


b) PLACYc Architecture Schematic Illustration. The Planetary Stage is Embedded in the Input Shaft of a Compact-Cam Cycloidal Reducer.

**Figure 1:** Schemes of the Planetary-Cycloidal Nested Series Reducers. The Acronyms Reported are Abbreviations for the Parts Illustrated with the Same Color. IN Refers to the Input Shaft (in Black), which is also the Sun of the Two planetary stages. The planets (P, in blue) are connected to the Planetary Carrier (PC, in light gray), which is fixed to FCB (i.e., the fixed Cycloidal Base, in Light Grey), to which the Rollers (R, in Light Green) are Connected. For the Compact-cam Design, the Rollers are Distinguished based on the Cycloidal base to which they are Connected. CD refers to the Cycloidal Disks (in Orange). In the Classic Double Disk Architecture, the Disks are Distinguished in CD1 and CD2, while the Compact-cam Disk is Addressed as CCD. The Output of the Two Reducers (OUT, in Green) Corresponds to the CC in PLACYd (i.e., the Cycloidal Carrier) and to CMB in PLACYc (Cycloidal Moving Base). The Output of the Planetary Stages (the Ring, R, in Red) also Represents the Cycloidal Eccentric Shaft (CES) is thus the Input Component for the two Cycloidal Stages.

### 2.1.2 Classic Cycloidal Drive Design

The operating principle of cycloidal reducers relies on the interaction of four primary components: an eccentric shaft that conveys the input motion from the motor, a cycloidal disk mounted on this shaft (or a pair of disks arranged on non-oppositely phased eccentric cams of the same shaft), a fixed ring comprising pins or rollers that constrains the disk's motion, and a set of output pins linked to the carrier, which collectively generate the output motion of the reducer. The term cycloidal stems from the characteristic geometry of the disk profile, which is derived from a cycloid curve (Yang et al., 2024). The reduction ratio of a classic Cycloidal drive is given by:

$$i_{cd} = \frac{(n_l - N_r)}{n_l} \tag{5}$$

where $n_l$ denotes the number of disk lobes, and $N_r$ represents the number of rollers. In the design of the PLACYd prototype, the cycloidal profiles were selected such that $n_l = N_r - 1$, ensuring proper meshing and obtaining the intended reduction characteristics. Therefore, the resulting reduction ratio can be computed as:

$$i_{cd} = \frac{1}{(1 - N_r)} \tag{6}$$

High reduction ratios in cycloidal mechanisms, while beneficial for axial compactness, introduce notable design challenges. As the target ratio increases, the number of rollers becomes larger, resulting in larger devices. Higher torques required at the output demand greater eccentricity, leading to an increasingly irregular motion. When combined with the need to transmit high torques, these effects may compromise robustness, requiring stiffer components, improved materials, and tighter alignment tolerances to ensure reliable operation. Thus, different solutions stem from the traditional cycloidal design, such as the double stage variant (Blagojevic et al., 2011) and the compact-cam architecture (Yang et al., 2024).

### 2.1.3 Cycloidal Compact-Cam Design

The compact-cam cycloidal architecture was introduced to further miniaturize transmission systems while maintaining high reduction ratios (Lin et al., 2022), removing the constraint between high reduction ratios and the number of rollers. This configuration reduces the radial encumbrance of the traditional cycloidal mechanism by

utilizing a single eccentric crankshaft and a pair of rigidly coupled cycloidal disks, thereby eliminating the need for a carrier, thus strongly simplifying the reducer's structure. As a result, high transmission ratios can be achieved within a compact radial envelope. The reduction ratio of a Cycloidal Compact-cam stage is defined as:

$$i_{cc} = \frac{(n_1 N_{r2} - n_2 N_{r1})}{(n_1 N_{r2})} \tag{7}$$

where $ni$ denotes the number of lobes on the disk at the $i$-th stage, and $N_{ri}$ represents the number of rollers at that stage. In the design of the PLACYc prototype, as for the classic cycloidal drive, the cycloidal profiles were selected such that $n_i = N_{ri} - 1$. A primary limitation of this architecture arises from the coupled constraints linking roller count and size, eccentricity, torque transmission capability, and backdrivability. The achievable output torque is fundamentally limited by the eccentricity and the number of rollers. Cycloidal disks with low eccentricity and few rollers are inherently unable to sustain high torques. Conversely, increasing the roller count or eccentricity compromises the simplicity of the design, resulting in higher mass, increased cost, and larger overall dimensions, and significantly degrades backdrivability. These effects are consistent with the performance trends observed in our previous evaluation of compact-cam prototypes (Bezzini et al., 2024).

### 2.2 PLACY Architecture

This work introduces a novel transmission architecture designed for wearable exoskeleton applications, representing an advancement of the previously developed hybrid Cycloidal-Planetary reducer. The proposed system integrates a compact planetary gearbox with a fixed carrier directly into the eccentric shaft of a cycloidal stage. The principal innovation lies in the spatial integration approach: the planetary reduction stage is concentrically embedded within the cycloidal shaft, enabling a substantial reduction in axial length while maintaining the mechanical performance of both stages. In this configuration, the output member of the planetary stage (i.e., the ring) coincides with the input element of the cycloidal stage (i.e., the shaft equipped with eccentric cams), effectively merging two functional components into a single structural part. This design constitutes an evolution of the prior Cycloidal-Planetary arrangement (Bezzini et al., 2024), preserving its advantageous characteristics while enhancing compactness, even at high reduction ratios, which is an essential requirement for actuators intended for wearable robotic devices.

The novel design implements a flat, nested configuration, wherein the planetary stage occupies the internal volume of the eccentric shaft, which is the input part of the successive cycloidal drive. This nesting strongly reduces the total axial dimension. Indeed, traditional cycloidal reducers display high radial encumbrances when implementing a high reduction ratio. As mentioned before, two different cycloidal architectures can be exploited for the implementation of the PLACY design: Two schematic cross-sectional illustrations of the proposed architectures are reported in Figure 1, where all the components are represented in different colors to facilitate the comprehension of the designs. This spatially efficient layout enables higher gear ratios to be implemented without increasing the gearbox axial encumbrance, a critical factor for applications demanding unobtrusive wearability. Moreover, unlike other architectures (such as the harmonic drive) that allow for high transmission ratios while maintaining a flattened shape, the PLACY design, through the series combination of a cycloidal and a planetary stage, is supposed to guarantee significant back drivability and low output impedance for improved transparency and user comfort in wearable robotics applications.

Considering the previously used nomenclatures, the reduction ratios for the two variants of the PLACY design (i.e., PLACYd for the one with classic cycloidal stage and PLACYc for the architecture involving the compact-cam variant) can be expressed respectively as:

$$i_{PLACYd} = i_{pl} \cdot i_{cd} = \frac{z_r}{z_s (N_r - 1)} \tag{8}$$

$$i_{PLACYc} = i_{pl} \cdot i_{cc} = z_r \frac{(N_{r2} - N_{r1})}{z_s (N_{r1} - 1) N_{r2}} \tag{9}$$

In summary, the proposed architecture seeks to merge the high reduction capability and low mechanical complexity, hence low mass and limited overall dimensions, characteristic of cycloidal mechanisms, with the superior torque transmission performance of spur gears. By nesting one stage within the other and employing a single component that serves simultaneously as the ring gear of the planetary stage and the input eccentric shaft of the cycloidal reducer, the axial footprint is substantially minimized. In this configuration, the remaining limit on axial dimensions is primarily dictated by the selection of rollers and bearings. Because the nested arrangement imposes stringent geometric and kinematic constraints on both stages, we introduce a practical design tool intended to assist in selecting suitable geometric parameters during the development of a PLACY reducer.

### 2.2.1 PLACY Geometric Design Tool

To facilitate and encourage the exploration and analysis of the proposed nested cycloidal-planetary architecture, we provide an executable tool and its source Python code at (Chen et al., 2008) for the geometric definition of custom PLACY reducers. Starting from the user's definition of the desired inner planetary stage ratio and maximum radial encumbrance, the proposed instrument first asks the user for the desired gear module. Then, the tool presents all the possible combinations of tooth numbers (and possible equivalently distant planet gears) to obtain the target $i$ (see Equation (4)). Once the planetary stage has been defined, given that the outer cycloidal stage stems from the ring gear (which will be the eccentric shaft), a radial constraint is defined for the encumbrance of the cycloidal drive (i.e., a maximum radial encumbrance for the overall reduction gearbox). The user at this point decides if the outer cycloidal stage should be a classic cycloidal drive or a compact-cam variant, thus choosing between a PLACYd and PLACYc transmission. The user then inserts the diameter of the rollers that should be used. Based on this feature and given the ring dimensions, the maximum and minimum number of rollers that can be employed for a cycloidal stage (be it a traditional cycloidal stage or a compact cam) is defined and employed to compute all the possible combinations of the number of rollers that can produce the desired reduction ratio.

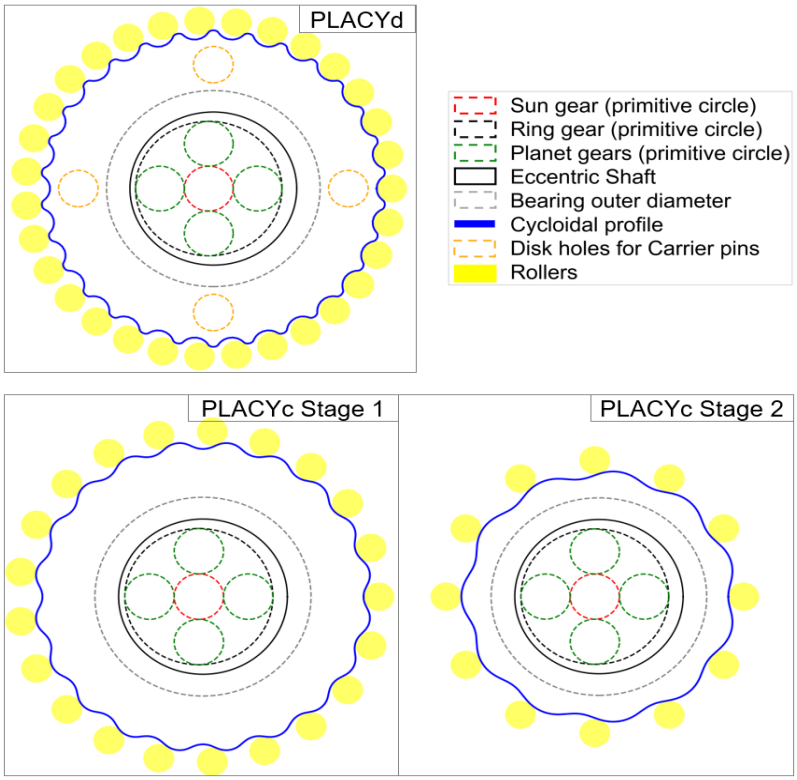


**Figure 2:** Example of the Output Figures from the Geometric Design Tool. Both Cases of PLACYd and PLACYc Designs are shown, with an Example of the Final Legend.

The remaining parameters (such as eccentricity, pitch diameters, diameter of the bearings to be used between the ring gear and cycloidal disks, and thickness of the ring-shaft component) for the cycloidal profile delineation are requested (and checked based on the mentioned restrictions). At this point, the resulting cycloidal geometry is arranged. The resulting cycloidal profiles and set of rollers are displayed through sketches, allowing the user to review their choices and optionally adjust some parameters. Once all the selected variables are confirmed, a sketched illustration shows the resulting view of the cycloidal stages arranged outside of the internal planetary gearbox (for simplicity, the sun, ring, and planets are represented through circles with a diameter equal to the primitive circles of the gears). An example of the final images in both PLACYd and PLACYc cases is displayed in Figure 2.

## 2.3 3D-Printed Prototypes

### 2.3.1 Design Assumptions and Constraints

The ultimate objective for the PLACY prototypes in terms of volume and mass was to significantly reduce the

axial encumbrance of the former CP30 and CP80 models, thereby achieving a transmission whose form factor approaches a flat configuration. In the previous Cycloidal Planetary reducers presented in (Bezzini et al., 2024), the two stages were arranged axially, resulting in relatively low radial encumbrance (78 mm in diameter). With the PLACY architecture, we also aim at minimizing horizontal expansion, as a flattened geometry, which is generally preferable for wearable assistive devices, is already embodied in the nested PLACY design; such a shape helps limit the overall increase in user volume when the exoskeleton is worn. Consequently, in alignment with earlier findings and current state-of-the-art benchmarks, we established prototype constraints of 80 mm for the diameter and 30 mm for the axial encumbrance. Regarding the target reduction ratio, we selected a value consistent with those investigated in our previous work to enable a fair comparison with the earlier prototypes. Additionally, given the intended application of the device in exoskeletons, a ratio of approximately 1:45 was deemed appropriate, as it is commonly adopted across multiple wearable systems (Calanca et al., 2022; Palazzi et al., 2022; Qiu et al., 2024).

### 2.3.2 Gearbox Design and Parameters

Using the procedure implemented in the available PLACY design tool, the design parameters of the presented prototypes were selected. These parameters are listed in Table 1 for both the PLACYd and PLACYc reducers. Both the final reducers provide an overall gear ratio of 1:45. This value offers adequate torque amplification when paired with compact electric motors, while maintaining low impedance and good backdrivability, features essential for safety and compliant behavior in human-exoskeleton interaction. The ratio is obtained through the combination of the internal planetary stage, which contributes with -1:3 multiplication, and cycloidal drives supplying a reduction of -1:15. The planetary stage was minimized in size, using both a low teeth module of 0.8 mm (which is the minimum for which the printed gears are guaranteed to present a well-defined profile, given the printers employed in this study) and the lowest number of teeth that guaranteed the dimensions needed for including bearings inside the planet gears (we employed W637 bearings, 2 x 2 x 4, between the planets and the carrier's pins. At the same time, the ring number of teeth was minimized to allow its inclusion inside the cycloidal shaft. The selected tooth configuration was chosen because it allowed an evenly spaced arrangement of a valid number of planets (four), in accordance with the condition:

$$\frac{(z_{\mathrm{s}} + z_{\mathrm{r}})}{n_{\mathrm{p}}} = I \tag{10}$$

where $n_p$ is the number of planets and $I \in Z$. The cycloidal profiles' parameters (i.e., roller diameter, eccentricity, and pith diameters) were defined through a trade-off between reasonable torque capability (sufficiently high eccentricity, number of rollers, and roller diameter), backdrivability (inversely proportional to the eccentricity), continuity and smoothness of the profiles, and limited target radial encumbrances. Two CAD sectional views of the resulting prototype are shown in Figure 3, using the same color scheme as Figure 1 to facilitate the identification and interpretation of the components. Exploded CAD views of the two prototypes are displayed in Figure 4. From the provided illustrations, it is clear that for the cycloidal stages of the PLACY transmissions, both the cycloidal disks and the outer rollers' profiles are composed of printed materials. Indeed, for the realization of the prototypes examined in this study, the nonpinwheel configuration has been employed, realizing the outer cycloidal profiles based on the formulas presented in (Ciobanu et al., 2025). This choice enabled highly lightweight and cost-effective gearboxes, avoiding the use of bearing rollers.

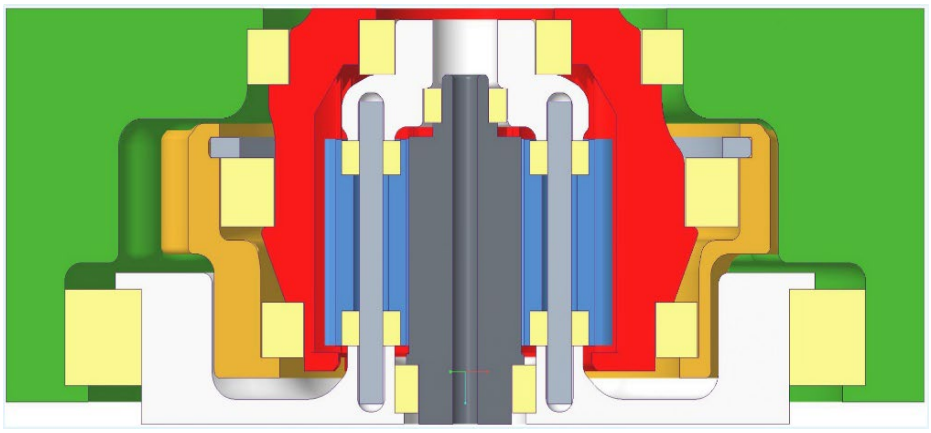

(a) Front Section CAD View of the PLACYd Prototype.

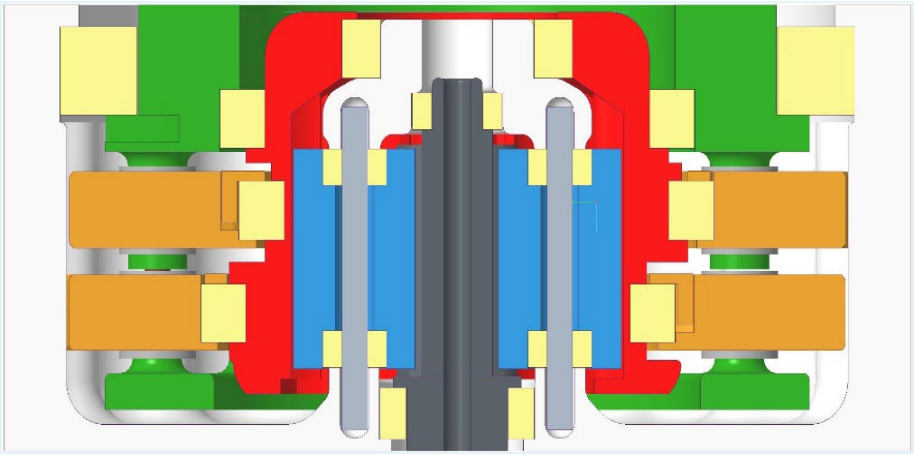

(b) Front Section CAD View of the PLACYc Prototype.

**Figure 3:** CAD Section Views of the PLACY Prototypes. The Colors Employed Match the Ones in Figure 1. Rollers, in Light Green, are the only Exception, since for the Two Presented Prototypes, the Non-pinwheel Architecture has been Employed, thus the Rollers' Cycloidal Profile is Composed of a Fully-printed Part, without Bearings. The Fixed Cycloidal base and the Fixed Planetary Carrier are Depicted in White. The Input Shaft with Sun Gear is in Black, while the Pins that Compose the Planetary Carrier on which the Planet Gears are Assembled are Represented in Light Grey. The Planets are Depicted in Blue. The Ring Gear (which is also the Cycloidal Eccentric Shaft) is Portrayed in Red. The structural Bearings Employed are Illustrated in Light Yellow. Both the Compact-cam and the Standard Cycloidal Disks are Represented in Orange. In (a), the Green Element (i.e., the Output) is the Moving Cycloidal base, while in (b), the Carrier is the Output Component Represented in Green.

**Table 1:** Design Parameters of the Presented PLACY 3D-printed Prototypes. S1 and S2 refer to the Compact-Cam Stages. For the PLACYd, the Parameters of the Cycloidal Stage are Expressed as those for Stage 1.

| | PLACYd | PLACYc | Description |
|---|---|---|---|
| $i_{pl}$ | -1:3 | -1:3 | Planetary stage Ratio |
| $z_r$ | 30 | 30 | Number of teeth Ring |
| $z_p$ | 10 | 10 | Number of teeth Planets |
| $n_p$ | 4 | 4 | Number of Planets |
| $z_s$ | 10 | 10 | Number of teeth Sun |
| $\alpha$ | 25° | 25° | Teeth pressure angle |
| $m$ | 0.8 mm | 0.8 mm | Teeth Module |
| $R_{cp}$ | 8 mm | 8 mm | Planetary Carrier Radius |
| $i_{cy}$ | -1:15 | -1:15 | Cycloidal stage Ratio |
| $D_{pr1}$ | 66 mm | 50 mm | Pitch Diameter (S1) |
| $N_{r1}$ | 16 | 8 | Number of rollers (S1) |
| $D_{pr2}$ | / | 60 mm | Pitch Diameter (S2) |
| $N_{r2}$ | / | 15 | Number of rollers (S2) |
| $D_r$ | 5 mm | 7 mm | Roller Diameter |
| $E$ | 1.5 mm | 1.5 mm | Eccentricity |
| $R_{cc}$ | 23.7 mm | / | Cycloidal Carrier Radius |
| $R_p$ | 3 mm | / | Carrier Pin Radius |
| $i_{tot}$ | 1:45 | 1:45 | Total Ratio |

### 2.3.3 Materials, Printers, and Components

To develop the PLACY prototypes, Ultimaker PLA and Ultimaker Nylon12-CF have been employed, given their valuable combination of low costs and significant mechanical properties (Ciobanu et al., 2025; Ciobanu et al., 2024). More precisely,PLA has been employed for the shaft and the gears that compose the planetary stage, while Nylon12CF has been used for both the cycloidal disks and the outer roller-like cycloidal profiles implementing the non-pinwheel

design. The use of the N12CF, given its significant mechanical properties, allowed for the cycloidal stages to be entirely realized in printed materials. The manufacturing process involved the use of the Ultimaker S7 Pro Bundle and the Ultimaker Method XL printers, with slicing carried out via Ultimaker Cura. The parts that were not produced through 3D printing are the bearings, screws, and nuts. CAD files and bills of materials are available upon request from the corresponding author.

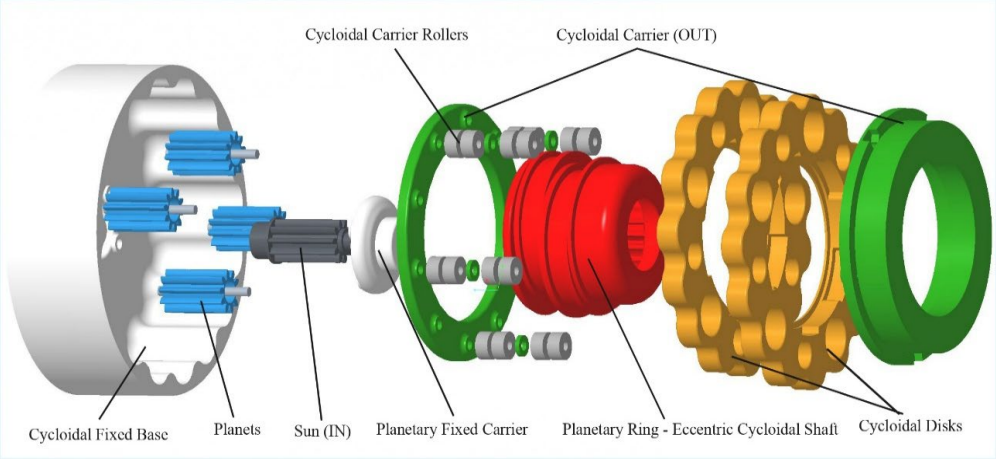


(a) Exploded CAD View of the PLACYd Prototype

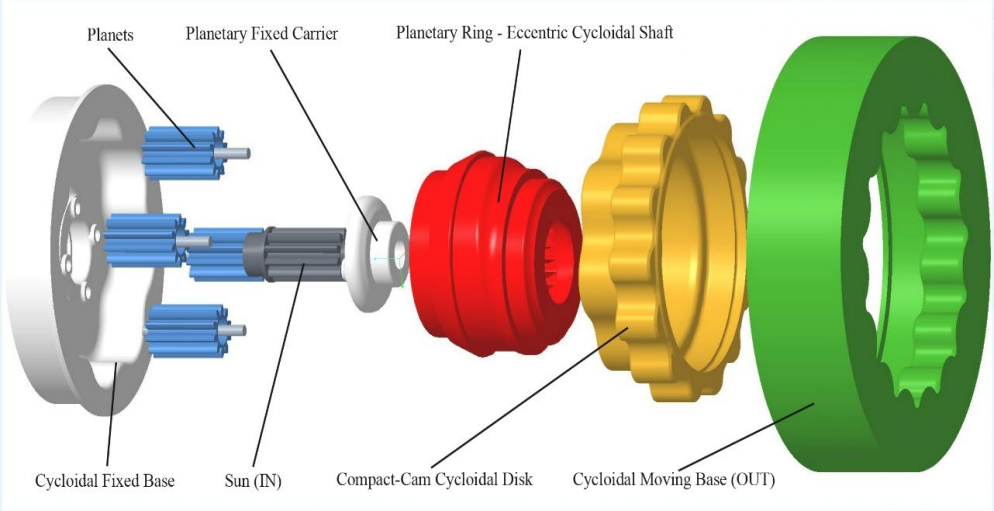


(b) Exploded CAD View of the PLACYc Prototype

**Figure 4:** The Colors Employed Match the Ones in Figure 1 and Figure 3 (Except for the Rollers, which in these Prototypes have been Replaced with a Non-pinwheel Profile). All the Main Components are Illustrated by the Notes. Structural Bearings, Screws, and Nuts have been Excluded from this Representation for the sake of Clarity. For the same Reason, the Cycloidal Moving Base (from the PLACYc) is Rendered as a Sectional View, to Clearly show the Internal Cycloidal Non-pin Wheel Profile. The Fixed Cycloidal base and the Fixed Planetary Carrier are Depicted in White. The Input Shaft with Sun Gear is in Black, While the Pins that Compose the Planetary Carrier on which the Planet Gears are Assembled are Represented in Light Grey. The Planets are Depicted in Blue. The Ring Gear (which is also the Cycloidal Eccentric Shaft) is Portrayed in Red. The Structural Bearings Employed are Illustrated in Light Yellow. Both the Compact-cam and the Standard Cycloidal Disks are Represented in Orange. In (b), the Green Element (i.e., the Output) is the Moving Cycloidal base, while in (a), the Carrier is the Output Component Represented in Green.

### 2.4 Experimental Evaluation

In this section, the two configurations of the experimental setup employed to evaluate the chosen metrics are

described. Then, the selected performance metrics are presented, together with the respective experimental protocols.

### 2.4.1 Experimental Setup

The experimental setup is composed of a brushless motor (EC 90 flat, 360 W, $\phi$ 90 mm, Maxon, Bad Homburg, Germany), which includes an integrated 2-channel encoder (MILE 512-6400 CPT, Maxon) coupled to the reducer's input shaft through the 3D-printed motor support. The reducer's output link is connected to an incremental magnetic encoder (H2 Series, Phoenix America, Fort Wayne, IN, USA) through the encoder support. All the mentioned components are fixed to a horizontal aluminum beam through a 3D-printed support structure. The motor-encoder assembly is controlled by a three-phase brushless DC motor driver (STEVAL-SPIN3201, STMicroelectronics, Geneva, Switzerland). The magnetic encoder and the two load cells (CZL635, Phidgets Inc.), which can be placed in a case on the output arm if the test demands the force detection at the reducer's output, are connected to the STM32 Nucleo-144 board (NUCLEO-F767ZI, STMicroelectronics). Both these boards are connected to the central unit (Intel NUC 11 Pro, i7-1165G7) running Windows 11 and Simulink (MATLAB, Mathworks Inc., Natick, MA, USA), where two PID (discrete PID controller, Simulink block) controls are designed to manage the motor's position and speed, depending on the performed test. A custom Kalman filter (Matlab function, Simulink block) is employed to estimate the motor speed.

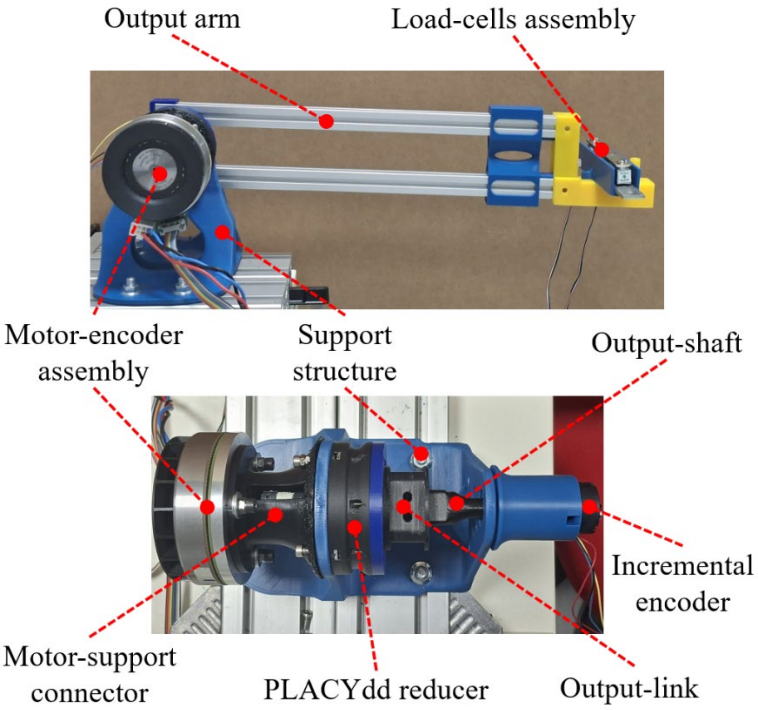


**Figure 5:** Experimental Setup Employed for Testing the Two PLACY Prototypes. The Two Photos and the Notes Clarify the Composition of the Experimental Setup, both in the Configuration with and without the Output Arm and the Load Cells.

Figure 5, where the main components are illustrated and pointed out, displays the setup with photos of the two exploited experimental arrangements. As can be seen from these photos, one configuration does not involve the use of the output arm, since the tests conducted in this arrangement did not include measurements of output forces or torques. The output arm is composed of two 20x20mm aluminum beams held together with some 3D-printed parts, which also include the terminal elements that are coupled with the load cells assembly employed for the tests under external loads.

### 2.4.2 Evaluation Metrics and Experimental Protocols

To evaluate the PLACYc and PLACYd prototypes' performance (and additionally compare them with the previous Cycloidal-Planetary series designs from (Bezzini et al., 2024)), the following metrics have been taken into consideration, defining the related experimental protocols to evaluate the key gearboxes' performance:

Friction: This quantity represents the motor torque required to overcome both static (Coulomb) and dynamic

(viscous) resistances opposing reducer motion. Accurately quantifying internal friction is essential for implementing compensation strategies, which in turn enhance the actuator's transparency in pHRI. The motor's internal static and viscous friction components were identified by commanding the actuator to track several velocity references. The resulting current measurements were employed to implement friction compensation in the following tests. More specifically, friction was characterized by applying slowly ramping speed references inputs within the range of ±100 rad/s, following the procedure described in (Roozing & Roozing, 2024). For a single test, six slowly ramping signals were employed, with low accelerations of ± 0.1, 0.2, 0.3 rad/s. The entire protocol was repeated three times for each PLACY reducer. Given the results reported in (Bezzini et al., 2024), the collected speed and torque data were initially used to attempt fitting the following friction model:

$$\tau_{fr} = \begin{cases} M_c^+ + d_v^+ \omega_m, & if\ \omega_m \geq 0 \\ -M_c^- + d_v^- \omega_m, & if\ \omega_m \leq 0 \end{cases} \quad (11)$$

where $\tau f\ r$ denotes the friction torque, $M{+}c$ and $M\ {-}c$ are the Coulomb friction components for positive and negative velocities, respectively, $d_v^+$ and $d_v^-$ are the viscous coefficients, and $\omega_m$ is the motor velocity. However, the experimental data did not conform to the model expressed in Equation (11). Consequently, a more detailed Stribeck-type friction formulation was adopted, expressed as:

$$\tau_{fr} = \sqrt{2e}(M_{brk} - M_c)e^{-\left(\frac{\omega}{\omega_{st}}\right)^2}\left(\frac{\omega}{\omega_{st}}\right) + M_c\ tanh\left(\frac{\omega}{\omega_{coul}}\right) + d\omega \quad (12)$$

with the characteristic velocities defined as

$$\begin{aligned} \omega_{st} &= \omega_{brk}\sqrt{2} \\ \omega_{coul} &= \omega_{brk}/10 \end{aligned} \quad (13)$$

where $M(v)$ is the friction moment as a function of the relative velocity $v$, $M_{brk}$ is the breakaway (stiction) friction force, $M_c$ denotes the Coulomb friction force, $\omega st$ represents the Stribeck velocity threshold, $\omega_{coul}$ the Coulomb friction threshold velocity, $\omega_{brk}$ the breakaway velocity, and $d$ the viscous friction coefficient. All these velocities (denoted by $\omega$) refer to the motor speed. This model captures the nonlinear decrease of friction from the breakaway value $M_{brk}$ toward the Coulomb level $M_c$ as velocity increases, with $\omega_{st}$ governing the Stribeck effect. At sufficiently high velocities, the viscous term $d$ becomes dominant, resulting in an approximately linear increase in friction. The presented model's parameters were identified by fitting the experimental data using MATLAB's *lsqcurvefit* nonlinear least-squares optimization function, which minimizes the squared error between the measured data and the model prediction. The suitability of the fitting procedure was assessed through the evaluation of the coefficient of determination $R^2$, to ensure the reliability and statistical robustness of the parameters' estimation.

Gear play: Defined as the output angular range of motion observable with the input shaft (i.e., the motor) locked, in which no resisting torque is transmitted from the actuator. A smaller gear play reflects higher positional accuracy in motion transmission, independently of the loads applied at the reducer's output. The gear play was quantified by measuring the maximum reducer's output displacement while keeping the motor's shaft blocked. To avoid the effect of joint stiffness on the gear play measurements, the procedure consisted of manually moving the reducer's output link without applying significant torque. The measurement was repeated at $i$ consecutive motor positions ($i$ being the reducer's reduction ratio), evenly spaced by an entire 360° motor rotation, to characterize the backlash over a full revolution of the reducer's output. Each prototype was tested three times to ensure consistency of the results.

Gear stiffness: The output stiffness of the gearbox is defined as the ratio between the applied output torque (with the input shaft locked) and the resulting angular displacement. This metric is significant because high stiffness improves tracking accuracy in trajectory-control tasks, whereas lower stiffness introduces compliance, which may be advantageous for smoother and safer physical human-robot interaction (pHRI). Thus, depending on the envisioned actuator's application, the stiffness characterization is essential for controlling properly the resulting device's interaction with the user. The experimental setup employed the output arm instrumented with load cells and configured with a lever arm length of 0.43 m. Transmission stiffness was identified by manually applying an increasing load to the arm while continuously measuring the load-cell force signal. Each loading sequence is referred to as GS in the following. The maximum applied torque for each reducer was approximately 30 Nm (this value also accounts for the torque generated by the weight of the arm and load-cell assembly). Testing the prototypes up to this target torque allows for an evaluation within a set of plausible values for wearable assistive exoskeletons such as (Kang et al., 2024; Luo et al., 2024).

Each test was repeated three times for the two reducers, with output positions incremented by approximately 30◦ to capture potential position-dependent variations. The resulting torque-displacement data were then used to fit a linear

model to estimate the output stiffness, defined as

$$k_g = \frac{\Delta\tau_{out}}{\Delta\theta_{out}} \tag{14}$$

where $k_g$ denotes the gearbox stiffness, $\Delta\tau_{out}$ is the applied output torque, and $\Delta\theta_{out}$ is the corresponding angular displacement. For each loading procedure (GSi) from 0 Nm to 30 Nm, the mean stiffness was computed, after which the mean value and standard deviation for each reducer were obtained. As for the friction model, the stiffness was identified by fitting the experimental data using MATLAB's *lsqcurvefit* optimization function, minimizing the squared error between the experimental data and the linear stiffness model. The validity of the fitting procedure was evaluated through the coefficient of determination $R^2$, to guarantee the soundness of the parameters' estimation.

Backdrive torque: The backdrive torque is defined as the external torque that must be applied at the output shaft to initiate motor motion. This quantity is particularly significant for wearable actuators, which should not impede the user's voluntary movements. The more an actuator can be back-driven by the user, the better the exoskeleton's transparency in the interaction with the wearer. The experimental setup used to characterize the backdrive torque employed both the output arm and the integrated load cells. At the start of each trial, the motor was positioned such that the output arm was horizontal, ensuring a consistent reference for compensating the torque contributions of the arm and load weight, which vary with the angular configuration. Increasing forces were then manually applied to the load cells until motor motion was detected. Each test was conducted at least five times and repeated across three independent sessions. The backdrive torque was estimated by identifying the onset of motor displacement, detected using a threshold of 0.18°, corresponding to twice the encoder resolution, and computing the associated applied torque. The final torque estimate accounted for both the manually applied forces and the torque contributions arising from the arm and load-cells weights, properly adjusted according to the output angle.

Speed Regularity: represents the oscillatory deviation between the monitored reducer output speed and its theoretical value. The latter is obtained as the product of the motor angular velocity and the transmission ratio. Assessing regularity provides insight into the stability and accuracy of speed transmission. The regularity metric quantifies the deviation between the actual output speed of the reducer and its theoretical value, providing a measure of the actuator's capability to track a certain velocity. To evaluate regularities ($R_{PLACYd}$ and $R_{PLACYc}$), a PID controller was employed to regulate the motor speed according to a sequence of step inputs ranging from 0 to ±120 rad/s in increments of 20 rad/s (Figure 8). For the two prototypes, each test was repeated three times for both positive and negative velocities. Regularity was then computed as:

$$R = 100\,(1 - \frac{\Delta\omega_g}{i\,\omega_m}) \tag{15}$$

where $R$ denotes the regularity (expressed as %), $\omega_g$ is the measured gearbox's output speed, $i$ represents the reduction ratio, and $\omega_m$ the motor speed.

Size and weight: The reducers were manufactured using Ultimaker PLA (polylactic acid) and Ultimaker Nylon12-Carbon Fiber. Consequently, the overall mass and volume depend on the relative proportion of PLA and NY12CF employed, as well as on the number and type of bearings and fasteners integrated into the assembly. Minimizing mass and bulk is crucial in wearable robotics, as it directly influences usability and user acceptance. Furthermore, achieving low manufacturing costs without compromising mechanical robustness is essential for enabling the widespread adoption of assistive technologies. These considerations motivated the previously discussed decision to resort to a fully printed no pinwheel configuration for the outer cycloidal profiles.

With regard to the prototypes' geometric encumbrance, the maximum height and diameter of each reducer were first extracted from the CAD models and subsequently validated through physical measurements. It is important to emphasize that the reported dimensions correspond solely to the gearbox bodies and do not include the mounting interface used in the experimental setup, which consists of four screws arranged on a 70 mm diameter bolt circle to secure both the motor support and the reducer to the printed fixture. As a result, the encumbrance comparison is independent of the test setup and instead reflects only the intrinsic design characteristics of the prototypes, enabling a fair comparison with other gearboxes presented in the literature. The total mass of each reducer was determined directly using a precision scale.

## 3. Results and Discussion

The torque (current multiplied by the motor torque constant) and velocity measurements from one representative friction test for each PLACY prototype, together with the corresponding fitted friction models, are shown in Figure 6.

The reported data clearly demonstrate that the Stribeck formulation was necessary to accurately capture the internal friction behavior of the gearbox. The parameter values employed in the Stribeck model to characterize the PLACY prototypes are listed in Table 2, alongside the parameters of the two Cycloidal-Planetary reducers presented in (Bezzini et al., 2024). The friction characterization for PLACYd and PLACYc achieved an $R^2$ value of 0.86 and 0.89, respectively, demonstrating a valuable consistency between the experimental data and the estimated models. It is important to note that, to ensure a fair comparison, the CP30 and CP80 parameters were reformulated according to the Stribeck model by using their original Coulomb static friction values as the breakaway component. Both the PLACY prototype exhibits higher static friction than the CP30 and CP80 devices, primarily because of the different contact dynamics attributable to the non-pinwheel printed profiles substituting the bearing-rollers, but also due to tighter tolerances that were intentionally adopted during the design to improve the gear-play limitations previously observed in the earlier reducers. This resulted in a slightly more demanding assembly process but improved overall mechanical quality. Nonetheless, despite being higher than the CP30 and CP80 values, the static friction of the PLACY prototypes remains substantially lower than that of other gearbox architectures reported in the literature (Roozing & Roozing, 2024; Seiler et al., 2024). The data also highlight the remarkably low viscous friction component, registered for both the proposed prototypes, but particularly significant in the PLACYd device, as further confirmed by the graphs in Figure 6, where friction visibly increases only marginally with velocity.

**Table 2:** Results from the Friction Tests. For the CP30 and CP80 Reducers, the Coulomb Static Friction has been Used as a Reference Breakaway Value, Since the Model Employed in (Bezzini et al., 2024) did not Include the Stribeck Breakaway Component.

| ID | Breakaway Friction [mNm] | Coulomb Friction [mNm] | Viscous Factor mNms/rad] |
|---|---|---|---|
| CP30 (Bezzini et al., 2024) | 13.4 ± 0.39 | 13.4 ± 0.39 | $1.16 \pm 0.09 \cdot 10^{-1}$ |
| CP80 (Bezzini et al., 2024) | 13.7 ± 0.75 | 13.7 ± 0.75 | $1.59 \pm 0.10 \cdot 10^{-1}$ |
| PLACYd | 60.7 ± 1.8 | 27.7 ± 1.1 | $0.154 \pm 0.043 \cdot 10^{-1}$ |
| PLACYc | 41.3 ± 1.3 | 25.1 ± 0.64 | $0.334 \pm 0.094 \cdot 10^{-1}$ |

The identified viscous coefficients (i.e., 0.154 ± 0.043 ·10−1 for the PLACYd and 0.334 ± 0.094 ·10−1 for the PLACYc) are notably small—especially when compared with state-of-the-art printed and metal gearboxes such as those in (Bezzini et al., 2024; Roozing & Roozing, 2024; Seiler et al., 2024), where the lowest reported viscous coefficient is $3.57 \times 10 - 5$ Nms/rad. These results indicate that the nested two-stage architecture constitutes a highly effective solution, as it roughly requires increased. As previously mentioned, tighter manufacturing tolerances were adopted relative to our prior work (Bezzini et al., 2024), which had adversely affected static breakaway and Coulomb friction, in order to enhance the CP30 and CP80 gear plays (1.1° and 0.89°, respectively). As shown in Table 3, the PLACY prototypes demonstrate a substantial reduction in gear play of approximately 86-94% compared to the previous devices, indicating a significant improvement. This performance also surpasses that of the 3D-printed cycloidal reducers reported in (Roozing & Roozing, 2024).

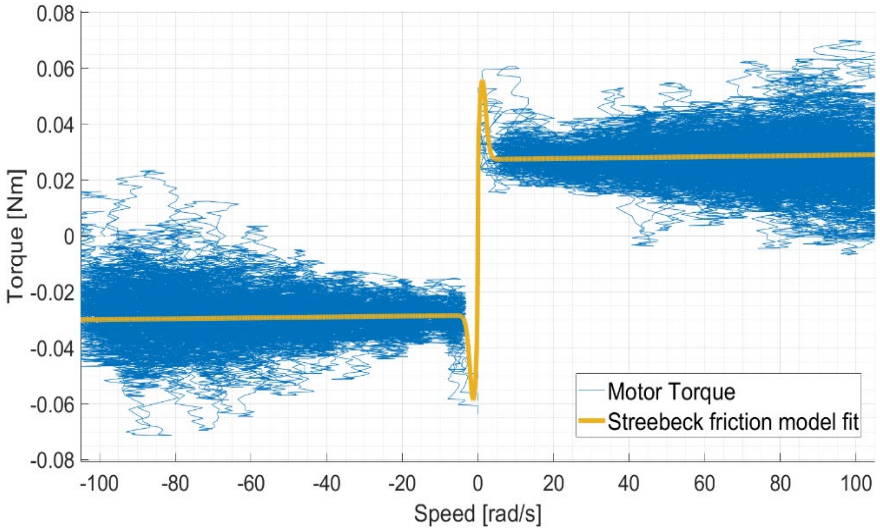


(a) Friction Data of PLACYc Prototype.

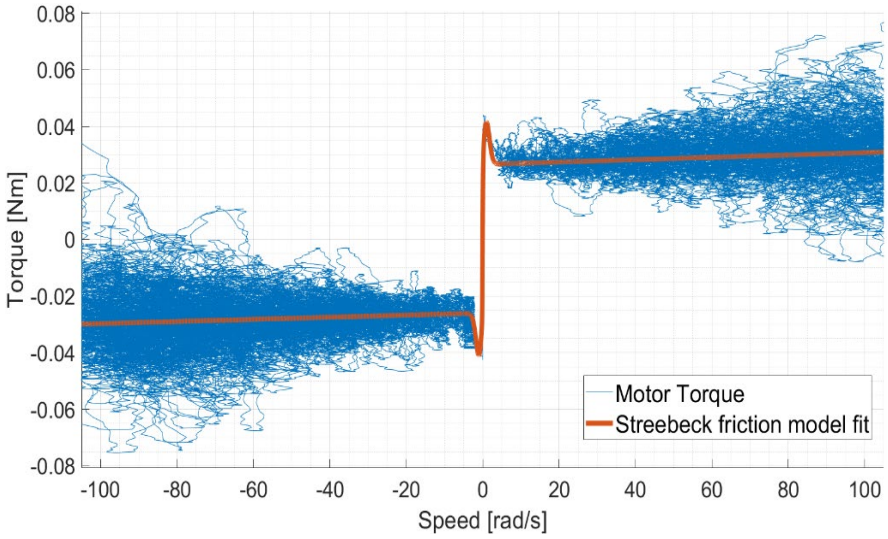


(b) Friction Data of PLACYd Prototype.

**Figure 6:** Example of Data from one of the Performed Friction Tests. The Motor Torque is Plotted with Respect to the Velocity. Also, the Stribeck Fitted Model for the Specific Experiment is Illustrated.

**Table 3:** Results from the Tests Regarding Gear Play, Gear Stiffness, and Backdrive Torque.

| ID | Gear Play [°] | Gear Stiffness [Nm/rad] | Backdrive Torque [Nm] |
|---|---|---|---|
| CP30 (Bezzini et al., 2024) | 1.1 ± 0.14 | 573.6 ± 59.52 | 0.59 ± 0.03 |
| CP80 (Bezzini et al., 2024) | 0.89 ± 0.23 | 472.5 ± 43.15 | 0.70 ± 0.04 |
| PLACYd | 0.121 ± 0.056 | 859.56 ± 55.62 | 1.39 ± 0.22 |
| PLACYc | 0.066 ± 0.029 | 918.07 ± 94.45 | 1.53 ± 0.49 |

**Table 4:** Regularity of the CP30, CP80, PLACYc, and PLACYd Reducers at the Investigated Motor Velocities. In the Last Column, the Overall Resulting Regularity is Reported.

| Motor Speed [rad/s] | 20 | 40 | 60 | 80 | 100 | 120 | R_TOT |
|---|---|---|---|---|---|---|---|
| CP30 (Bezzini et al., 2024) Regularity [%] | 95.5 | 94.8 | 95.77 | 95.85 | 94.87 | 96.25 | 95.51 ± 0.57 |
| CP80 (Bezzini et al., 2024) Regularity [%] | 95.9 | 96.88 | 94.9 | 94.35 | 95.51 | 95.68 | 95.54 ± 0.87 |
| PLACYd Regularity [%] | 96.41 | 95.21 | 95.28 | 95.48 | 95.51 | 95.39 | 95.56 ± 0.50 |
| PLACYc Regularity [%] | 95.32 | 93.31 | 93.79 | 93.91 | 93.78 | 93.69 | 93.84 ± 0.42 |

Regarding the gearbox stiffness, it is worth noting that multiple details in the design and manufacturing of the presented prototype aimed at improving the reducer's rigidity with respect to the CP30 and CP80 prototypes: the use of Nylon12CarbonFiber for the cycloidal disks and outer non-pinwheel profiles and the use of steel pins for the planetary carrier bars module for the planetary gears, and the use of steel pins for reinforcing the planetary carrier's rigidity. Given these features, as confirmed by the values reported in Table 3, the PLACYc and PLACYd prototypes display a significant increase in stiffness, reaching values of 918.07 Nm/rad and 859.56 Nm/rad, respectively.

The regression models employed to evaluate the stiffness reached $R^2$ values of 0.83 and 0.84 for PLACYc and PLACYd, respectively, indicating a strong correspondence between the experimental measurements and the fitted trend. These results indicate a highly reduced elastic deformation under the action of output torques, contributing to enhanced control precision and dynamic responsiveness and thus confirming the effectiveness of the proposed architectures in minimizing mechanical compliance. The resulting PLACy stiffness is also higher than the values estimated for all the reducers from our previous work (Bezzini et al., 2024). Moreover, taking as a reference state-of-the-art compliant actuators (Hussain et al., 2026; Sandeep Reddy et al., 2025; Satheeshbabu et al., 2025), the resulting stiffness values are confirmed to be worthwhile in multiple applications, including wearable robotics. As a more direct

demonstration of the resulting stiffnesses, Figure 7 illustrates the applied torques and resulting angular deflection during one of the loading phases GS of a stiffness test for both of the presented prototypes. From these images, the linear relation between torque and deflection is quite evident.

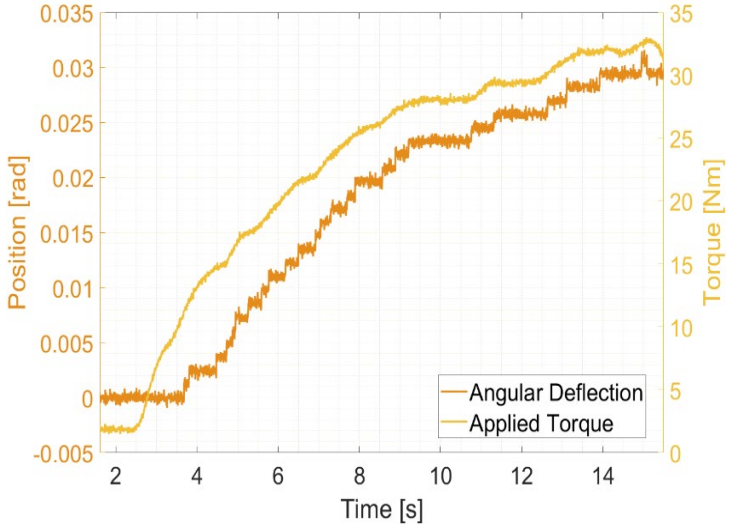


(a) Torque and Position Data from one of the Loading Phases GS of a Stiffness Test for the PLACYd Prototype.

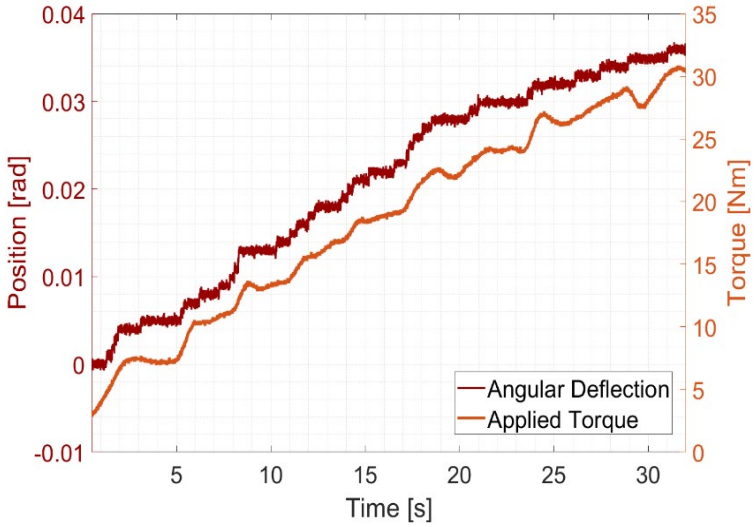


(b) Torque and Position data from one of the Loading Phases GS of a Stiffness Test for the PLACYc Prototype.

**Figure 7:** Example of Data from one of the Performed Stiffness Tests During one of the Three Loading Phases for both the Presented PLACY Prototypes. The Applied Torques (Right y-axis) and the Output Angular Deflections (Left y-axis) are Illustrated with Respect to Time.

Regarding backdrive torque, the observed increase in internal friction inevitably results in higher torque requirements to initiate motor motion from the gearbox output side. Nonetheless, the calculated backdrive torques of 1.39 Nm for the PLACYd and 1.53 Nm for the PLACYc remain beneficial for wearable devices. Not only are these values comparable (if not lower) with those reported for other reducers used in wearable exoskeletons (Seiler et al., 2024; Yu et al., 2020), but they also represent a negligible fraction of the reducer's torque capacity (35 Nm), corresponding to only 3% of the maximum allowable output torque. Regarding the speed regularity of the PLACY prototypes, the results obtained across all tested motor velocities, together with the overall regularity metric, are reported in Table 4, where the best-performing values among the CP30, CP80, and PLACY reducers are highlighted in bold characters. All devices exhibit consistently high motion regularity throughout the entire velocity range, with

mean values exceeding 95%, with the exception of the PLACYc gearbox, whose regularity emerges as slightly inferior (with an $R_{TOT}$ equal to 93.84 %). This is mainly due to the employment of the Compact-cam architecture, whose limitation in terms of speed regularity already emerged in previous works (Bezzini et al., 2024).

Despite the minor weakness of PLACYc (whose resulting regularity is still higher than that of the compact-cam drives of (Bezzini et al., 2024)), the PLACY architecture displays a smooth and stable torque transmission with limited kinematic error. Among them, the PLACYd prototype achieves the highest average regularity (95.56 ± 0.5 %), slightly outperforming the earlier Cycloidal-Planetary designs. These findings confirm that the design choices in the compact-cam stage eccentricity, roller diameter, and pitch circumferences effectively mitigate the kinematic irregularities associated with backlash and transmission nonlinearities. Such performance is especially advantageous in wearable robotic applications, where velocity smoothness directly affects user comfort, control fidelity, and overall transparency. Additionally, the minimal variation in regularity across velocities highlights the robustness and stability of the proposed architecture for dynamic scenarios.

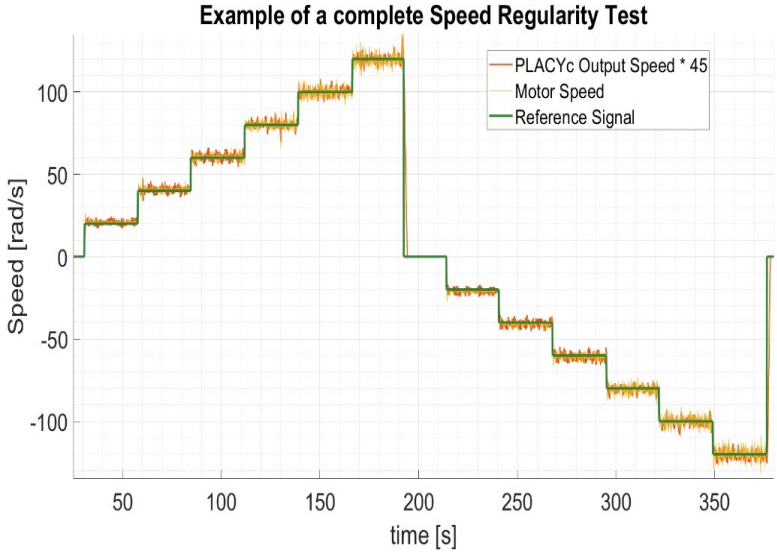


**Figure 8:** Data from One of the Performed Speed Regularity Tests. The Reference Signal is Represented in Green, and it Consists of a Series of Speed Steps (from 0 rad/s to ±120 rad/s, with Steps of 20 rad/s). The Motor and the PLACYc Gearbox's Output Speeds (the Latter was Multiplied by the Inverse of the Reduction Ratio, i.e., 45, to Plot it Together with the Motor's Speed and the Reference Signal) are Plotted, respectively, in Yellow and Red.

The dimensions (maximum diameter and height) and weights of the PLACY prototypes are summarized in Table 5, together with the corresponding data reported in (Bezzini et al., 2024) for the CP30 and CP80 gearboxes. For completeness, the best-performing values are highlighted in bold. Regarding the axial encumbrance, the novel nested Planetary-Cycloidal concentric configuration demonstrated its effectiveness by establishing a strict upper bound on the reducer height, independent of the selected transmission ratio. The resulting 30 mm height for both the reducers is markedly lower than that of all eight reducers presented in (Bezzini et al., 2024), and also compares favorably with other 3D-printed and metal-built architectures described in (Hur et al., 2023; Yoshida et al., 2023; Yu et al., 2020).

**Table 5:** Encumbrances (Maximum Diameter and Height), Weight, and Cost of the Presented Reducers

| ID | Diameter [mm] | Height [mm] | Weight [g] |
|---|---|---|---|
| CP30 (Bezzini et al., 2024) | 78 | 52 | 272 |
| CP80 (Bezzini et al., 2024) | 78 | 52 | 302 |
| PLACYd | 74.2 | 30 | 181 |
| PLACYc | 70.5 | 30 | 154 |

Although the flat arrangement may require an increased diameter depending on the cycloidal and planetary stage parametrization and the target reduction ratio, these PLACY prototypes maintain a comparatively low radial footprint, moreover remaining under the diameter of the previous CP gearboxes. Many existing transmissions exhibit substantially larger encumbrances even when designed for lower transmission ratios (Roozing & Roozing, 2024).

With respect to mass, which is an essential parameter for wearable robotics due to its direct influence on comfort and user acceptance, the PLACY prototypes exhibit a significantly reduced weight compared to the CP30 and CP80 devices. This improvement can be attributed both to the adoption of a small modulus for the planetary gearset and the employment of non-pinwheel cycloidal stages, which minimize the number of required components relative to a classical cycloidal design, where the rollers are usually bearings. Consequently, the proposed reducer achieves a notably lower mass than other solutions reported in the literature (Bezzini et al., 2025; Roozing & Roozing, 2024; Yoshida et al., 2023; Yu et al., 2020). Furthermore, based on the scoping review in (Bettella et al., 2025) concerning transmission systems used in exoskeletons, the overall mass of the evaluated PLACY devices places it well below the lower bound of the weight range documented for comparable reducers. Finally, even considering the classic employment of bearings as rollers (and the consequent necessity of screws and nuts for keeping them on the pitch diameter) in the proposed PLACY gearboxes, a plausible increase of approximately 45 g for the PLACYd and 70 g for the PLACYc still would lead to notably lower weights then the average gearboxes for wearable devices according to (Bettella et al., 2025).

### 3.1 Overall Considerations

The comparative evaluation of the PLACYc and PLACYd reducers against the CP30 and CP80 models shows consistent performance gains across all relevant metrics for wearable robotic actuation. Although the PLACY prototypes exhibit higher breakaway and Coulomb friction due to tighter tolerances and the adoption of non-pinwheel profiles, their overall friction remains substantially lower than that of many state-of-the-art printed and metal gearboxes. Moreover, both designs feature remarkably low viscous friction, particularly the PLACYd, therefore confirming the efficiency of the nested architecture in maintaining smooth behavior and preserving torque capacity across higher speeds. The most significant improvements concern gear play and stiffness. The PLACY prototypes achieve an 86-94% reduction in gear play relative to CP30 and CP80 and show a marked increase in stiffness (918 Nm/rad for PLACYc and 860 Nm/rad for PLACYd), resulting in reduced elastic deformation and improved control precision. Speed-regularity tests further demonstrate stable and smooth transmission, with the PLACYd achieving the highest overall regularity (95.56%) among all evaluated reducers. In terms of space integration in plausible wearable exoskeletons, the PLACY architecture offers a substantially reduced axial height (30 mm) and lower weight (154 g for PLACYc and 181 g for PLACYd), making both prototypes well-suited for compact wearable actuators. Despite the increased static friction, backdrive torque remains low (1.39-1.53 Nm, almost 3% of rated torque capacity), ensuring good transparency for a safe human-robot interaction. Overall, the PLACYc and PLACYd combine low friction, high stiffness, reduced backlash, strong regularity, and minimal encumbrance, outperforming the CP series and offering a competitive alternative to current printed and metal-built gearbox solutions for wearable robotics. The proposed evaluation does not take into account possible durability issues, which may be caused by the use of 3D-printed materials. However, previous studies on both 3D-printed cycloidal drives (Olejarczyk et al., 2026; Roozing & Roozing, 2024) and classic gears (Ciobanu et al., 2024) provide insights from degradation studies and fatigue tests, corroborating the use of printed components in transmission systems for robotics through positive evaluation of the durability of these parts.

## 4. Conclusions

This work introduced a novel nested Planetary-Cycloidal concentric nested architecture designed to improve actuation in assistive exoskeletons by enabling flat, compact, and lightweight gearboxes even at high transmission ratios. Two 3D-printed PLACY prototypes, implementing different variants of the proposed design, were developed and experimentally characterized to validate the proposed concept. Motivated by the limitations of existing reducers, typically exhibiting excessive axial size, insufficient stiffness, limited backdrivability, and elevated weight, the PLACY architecture integrates a compact planetary stage within a cycloidal drive's eccentric shaft, achieving high reductions within a low-profile, lightweight form factor. A thorough experimental evaluation of the 1:45 PLACY prototypes was conducted, assessing frictional properties, speed regularity, stiffness, gear play, and backdrivability using standardized protocols that enable direct comparison with prior Cycloidal-Planetary designs and state-of-the-art transmissions. The results indicate that the proposed architecture provides a balanced combination of efficiency, compactness, smoothness, and mechanical performance across all tested metrics, making it a strong candidate for wearable and assistive robotic applications. Its modularity further supports adaptation to various joint geometries, facilitating the development of lightweight and cost-effective actuation units. To promote adoption, a geometric design tool and its source code are openly provided. Future developments will focus on fabricating metal variants to increase load capacity, refining the geometry to reduce encumbrance in smaller-scale versions further, and integrating the reducer into a complete exoskeleton for an exhaustive evaluation during human-assistive tasks. In addition, the design tool will be expanded to incorporate theoretical performance models, providing users with predictive information on

the impact of design choices on gearbox behavior with respect to key transmission metrics.

## 5. Funding Data

The purchase of the materials used in this work and part of the personnel costs were supported by the BRIEF "Biorobotics Research and Innovation Engineering Facilities" project (Project identification code IR0000036) funded under the National Recovery and Resilience Plan (NRRP), Mission 4 Component 2 Investment 3.1 of the Italian Ministry of University and Research, funded by the European Union - NextGenerationEU.

Part of the activities and personnel of this work were supported by the Department of Excellence in Robotics and AI, funded by the Ministry of Research and University (DM 230/2022).

## References

Barsomian, C., Eswaran, N., Pesenti, M., Gandolla, M., Braghin, F., Carpanzano, E., & Roveda, L. (2024). Dynamic characterization and control of a back-support exoskeleton 3D-printed cycloidal actuator. *CIRP annals*, *73*(1), 29-32. https://doi.org/10.1016/j.cirp.2024.03.002

Bettella, F., Tortora, S., Menegatti, E., Petrone, N., & Del Felice, A. (2025). A scoping review on lower limb exoskeleton actuation's description and characteristics. *Robotica*, 1-18. https://doi.org/10.1017/S0263574725000220

Bezzini, R., Bassani, G., Avizzano, C. A., & Filippeschi, A. (2024). Design and experimental evaluation of multiple 3D-printed reduction gearboxes for wearable exoskeletons. *Robotics*, *13*(11), 168. https://doi.org/10.3390/robotics13110168

Bezzini, R., Bassani, G., Avizzano, C. A., & Filippeschi, A. (2025). Design of a Novel Flat Cycloidal-Planetary Series Reducer and Experimental Assessment for Assistive Exoskeletons Actuation-CYPLO. *IEEE Access*, *13*, 202619-202631. https://doi.org/10.1109/ACCESS.2025.3638162

Blagojevic, M., Marjanovic, N., Djordjevic, Z., Stojanovic, B., & Disic, A. (2011). A New Design of a Two-Stage Cycloidal Speed Reducer. *Journal of mechanical design*, *133*(8). https://doi.org/10.1115/1.4004540

Calanca, A., Dimo, E., Palazzi, E., & Luzi, L. (2022). Enhancing force controllability by mechanics in exoskeleton design. *Mechatronics*, *86*, 102867. https://doi.org/10.1016/j.mechatronics.2022.102867

Calanca, A., Toxiri, S., Costanzi, D., Sartori, E., Vicario, R., Poliero, T., Di Natali, C., Caldwell, D. G., Fiorini, P., & Ortiz, J. (2020). Actuation selection for assistive exoskeletons: matching capabilities to task requirements. *IEEE Transactions on Neural Systems and Rehabilitation Engineering*, *28*(9), 2053-2062. https://doi.org/10.1109/TNSRE.2020.3010829

Chen, B., Fang, T., Li, C., & Wang, S. (2008). Gear geometry of cycloid drives. *Science in China Series E: Technological Sciences*, *51*(5), 598-610. https://doi.org/10.1007/s11431-008-0055-3

Ciobanu, R., Arhip, G., Donțu, O., Rizescu, C. I., & Grămescu, B. (2025). Additive manufacturing meets gear mechanics: Understanding abrasive wear evolution in FDM-printed gears. *Polymers*, *17*(13), 1810. https://doi.org/10.3390/polym17131810

Ciobanu, R., Rizescu, C. I., Rizescu, D., & Gramescu, B. (2024). Surface durability of 3D-printed polymer gears. *Applied Sciences*, *14*(6), 2531. https://doi.org/10.3390/app14062531

Fan, W., Dai, Z., Zhang, B., He, L., Pan, M., Yi, J., & Liu, T. (2024). HyExo: A novel quasi-passive hydraulic exoskeleton for load-carrying augmentation. *IEEE/ASME Transactions on Mechatronics*, *30*(1), 144-155. https://doi.org/10.1109/TMECH.2024.3391350

Hartnett, R. J., Berdal, J. B., & Quintero, D. (2025). Design of a Modular Rotary Actuator Characterization Test Station for Wearable Robotics. In *2025 IEEE 21st International Conference on Automation Science and Engineering (CASE)* (pp. 2574-2579). IEEE. https://doi.org/10.1109/CASE58245.2025.11163978

Huang, T.-H., Zhang, S., Yu, S., MacLean, M. K., Zhu, J., Di Lallo, A., Jiao, C., Bulea, T. C., Zheng, M., & Su, H. (2022). Modeling and stiffness-based continuous torque control of lightweight quasi-direct-drive knee exoskeletons for versatile walking assistance. *IEEE Transactions on Robotics*, *38*(3), 1442-1459. https://doi.org/10.1109/tro.2022.3170287

Hur, S., Kim, D., Lee, C., & Choi, D. (2023). Optimal design of a compound planetary reducer using a nonlinear optimization method. *IEEE Access*, *11*, 7822-7828. https://doi.org/10.1109/ACCESS.2023.3238579

Hussain, I., Turki Almansoori, M., Tamaizi, K., Albalasie, A., Niu, Z., & Gan, D. (2026). Design, Modeling, Evaluation, and Control of a Compact Discrete Variable Stiffness Actuator. *Journal of Mechanisms and Robotics*, *18*(2), 020903. https://doi.org/10.1115/1.4069904

Jenks, B., Levan, H., & Stefanovic, F. (2025). OpenSEA: a 3D printed planetary gear series elastic actuator for a compliant elbow joint exoskeleton. *Frontiers in Robotics and AI*, *12*, 1528266. https://doi.org/10.3389/frobt.2025.1528266

Kang, O., Yun, J., Seo, S., Joe, H.-M., Yi, H., & Lee, S. (2024). A novel design of unpowered exoskeleton for loaded walking using only hip abduction torque. *IEEE/ASME Transactions on Mechatronics*, *29*(4), 2534-2544. https://doi.org/10.1109/TMECH.2023.3333339

Karthik, V., Das, S., Nayak, S., & Pandey, A. (2025). Lower Limb Exoskeletons, Application-Centric Classifications: A Review. *Journal of Field Robotics*, *42*(6), 2397-2411. https://doi.org/10.1002/rob.22529

Laschowski, B., & McPhee, J. (2023). Energy-efficient actuator design principles for robotic leg prostheses and exoskeletons: A review of series elasticity and backdrivability. *Journal of Computational and Nonlinear Dynamics*, *18*(6), 060801. https://doi.org/10.1115/1.4056919

Lin, T.-C., Schabacker, M., Ho, Y.-L., Kuo, T.-C., & Tsay, D.-M. (2022). Geometric design and dynamic analysis of a compact cam reducer. *Machines*, *10*(10), 955. https://doi.org/10.3390/machines10100955

Luo, S., Jiang, M., Zhang, S., Zhu, J., Yu, S., Dominguez Silva, I., Wang, T., Rouse, E., Zhou, B., & Yuk, H. (2024). Experiment-free exoskeleton assistance via learning in simulation. *Nature*, *630*(8016), 353-359. https://doi.org/10.1038/s41586-024-07382-4

Maccioni, L., Concli, F., & Blagojevic, M. (2023). A new three-stage gearbox concept for high reduction ratios: Use of a nested-cycloidal architecture to increase the power density. *Mechanism and Machine Theory*, *181*, 105203. https://doi.org/10.1016/j.mechmachtheory.2022.105203

Matsuki, H., Nagano, K., & Fujimoto, Y. (2019). Bilateral drive gear—a highly backdrivable reduction gearbox for robotic actuators. *IEEE/ASME Transactions on Mechatronics*, *24*(6), 2661-2673. https://doi.org/10.1109/TMECH.2019.2946403

Mišković, L., Dežman, M., & Petrič, T. (2024). Pneumatic exoskeleton joint with a self-supporting air tank and stiffness modulation: Design, modeling, and experimental evaluation. *IEEE/ASME Transactions on Mechatronics*, *29*(5), 3415-3426. https://doi.org/10.36227/techrxiv.21988589.v1

Olejarczyk, K., Wikło, M., & Rucki, M. (2026). Analysis of 3D-Printed Cycloidal Gear Degradation in a Run-to-Failure Test. *Applied Sciences*, *16*(6), 2866. https://doi.org/10.3390/app16062866

Palazzi, E., Luzi, L., Dimo, E., Meneghetti, M., Vicario, R., Luzia, R. F., Vertechy, R., & Calanca, A. (2022). An affordable upper-limb exoskeleton concept for rehabilitation applications. *Technologies*, *10*(1), 22. https://doi.org/10.3390/technologies10010022

Qian, Y., Han, S., Wang, Y., Yu, H., & Fu, C. (2022). Toward improving actuation transparency and safety of a hip exoskeleton with a novel nonlinear series elastic actuator. *IEEE/ASME Transactions on Mechatronics*, *28*(1), 417-428. https://doi.org/10.1109/TMECH.2022.3201255

Qiu, J., Dong, L., Guo, R., He, Y., Cheng, H., & Li, W. (2024). Multi-terrain adaptive control for knee exoskeletons: Development and experimental evaluation. In *2024 China Automation Congress (CAC)* (pp. 1658-1663). IEEE. https://doi.org/10.1109/CAC63892.2024.10864914

Rodríguez-Jorge, D., Zhang, S., Huang, J. S., Lopez-Sanchez, I., Srinivasan, N., Zhang, Q., Zhou, X., & Su, H. (2025). Biomechanics-informed mechatronics design of comfort-centered portable hip exoskeleton: actuator, wearable interface, controller. *IEEE Transactions on Medical Robotics and Bionics*. https://doi.org/10.1109/TMRB.2025.3560394

Roozing, W., & Roozing, G. (2024). Experimental comparison of pinwheel and non-pinwheel designs of 3D-printed cycloidal gearing for robotics. In *2024 IEEE International Conference on Robotics and Automation (ICRA)* (pp. 7091-

7098). IEEE. https://doi.org/10.1109/ICRA57147.2024.10610250

Sandeep Reddy, M., Rakshit, S., & Sujatha, S. (2025). A New Adjustable Stiffness Rotary Series Elastic Actuator Based on Lockable Spring Elements. *Journal of Mechanisms and Robotics*, *17*(12), 121005. https://doi.org/10.1115/1.4069720

Satheeshbabu, S., Puduchatiram Raman, E., Krishnan, G., & Patiballa, S. K. (2025). Design of Compliant Systems With Embedded Actuation. *Journal of Mechanisms and Robotics*, *17*(12), 124501. https://doi.org/10.1115/1.4070087

Seiler, J., Schäfer, N., Zhao, G., Latsch, B., Grimmer, M., Beckerle, P., & Kupnik, M. (2024). Human-Exoskeleton Interaction Force Estimation Based on Quasi-Direct Drive Actuators. In *2024 10th IEEE RAS/EMBS International Conference for Biomedical Robotics and Biomechatronics (BioRob)* (pp. 1132-1139). IEEE. https://tinyurl.com/5n7eut8w

Tiboni, M., Borboni, A., Vérité, F., Bregoli, C., & Amici, C. (2022). Sensors and actuation technologies in exoskeletons: A review. *Sensors*, *22*(3), 884. https://doi.org/10.3390/s22030884

Xia, Y., Wei, W., Lin, X., & Li, J. (2024). Optimization of torque-control model for quasi-direct-drive knee exoskeleton robots based on regression forecasting. *Sensors*, *24*(5), 1505. https://doi.org/10.3390/s24051505

Xu, S., Tang, K., Xu, L., & Ding, Y. (2025). Design, analysis, and validation of a passive parallel continuum ankle exoskeleton for support and walking assistance. *Journal of Mechanisms and Robotics*, *17*(3), 031003. https://doi.org/10.1115/1.4066136

Yang, H., Li, Y., Huang, J., Li, X., & Sun, L. (2024). Theoretical analysis and performance prediction of a NN-type precision cycloidal reducer. *Forschung im Ingenieurwesen*, *88*(1), 44. https://doi.org/10.1007/s10010-024-00763-1

Yang, Y., Zhou, G., Chang, L., & Chen, G. (2021). A modelling approach for kinematic equivalent mechanism and rotational transmission error of RV reducer. *Mechanism and Machine Theory*, *163*, 104384. https://doi.org/10.1016/j.mechmachtheory.2021.104384

Yoshida, T., Endo, G., Okubo, A., & Nabae, H. (2023). Experimental Evaluation of a Quasi-direct-drive Actuator with a 3D-printed Planetary Gear Reducer. In *2023 IEEE/SICE International Symposium on System Integration (SII)* (pp. 1-6). IEEE. https://doi.org/10.1109/SII55687.2023.10039274

Yu, S., Huang, T.-H., Yang, X., Jiao, C., Yang, J., Chen, Y., Yi, J., & Su, H. (2020). Quasi-direct drive actuation for a lightweight hip exoskeleton with high backdrivability and high bandwidth. *IEEE/ASME Transactions on Mechatronics*, *25*(4), 1794-1802. https://doi.org/10.1109/tmech.2020.2995134

Zhu, L., Cui, C., Zhang, D., Tan, J., & Xu, C. (2025). Modeling and Control of Cable-Driven Exoskeleton for Arm Rehabilitation. *Journal of Mechanisms and Robotics*, *17*(6), 061010. https://doi.org/10.1115/1.4067305